Hamburger Beiträge
zur Angewandten Mathematik

Algebraic Medical Image Reconstruction from Scattered Radon Data by Positive Definite Kernel

Stefano De Marchi, Armin Iske, Amos Sironi

Nr. 2012-08
June 2012

Algebraic Medical Image Reconstruction from Scattered Radon Data by Positive Definite Kernels

Stefano De Marchi
Department of Mathematics, University of Padua, Italy
demarchi@math.unipd.it

Armin Iske
Department of Mathematics, University of Hamburg, Germany
iske@math.uni-hamburg.de

Amos Sironi
CVLab, EPFL, Lausanne, Switzerland
amos.sironi@epfl.ch

June 1, 2012

Abstract

Computerized tomography requires customized numerical methods for the approximation of a bivariate target function f from a finite set of discrete Radon data, each of whose data samples represents one line integral of f. In standard reconstruction methods, specific assumptions concerning the distribution of the sample lines are usually made, e.g. by parallel line geometry. In relevant applications of medical image reconstruction, however, such assumptions are often too restrictive. In this case, one would rather prefer to work with reconstruction methods allowing for arbitrary distributions of scattered sample lines.

In this paper, we propose a novel kernel-based algebraic reconstruction method for medical image reconstruction from scattered Radon data. Our reconstruction relies on generalized Hermite-Birkhoff interpolation by positive definite kernel functions in combination with a suitable regularization of the Radon transform. This leads to a very flexible reconstruction method for medical images, whose good performance is supported by numerical examples and comparisons with classical Fourier-based methods relying on the filtered back projection formula.

Keywords: Medical image reconstruction, computerized tomography, algebraic reconstruction techniques, Hermite-Birkhoff interpolation, positive definite kernel functions.

1 Introduction

Computed Axial Tomography (CAT or CT) is a powerful technique to generate (medical) images from measurements of X-ray scans. One X-ray scan typically consists of several million of data samples, each of which corresponds to an X-ray beam passing through the computational domain, traveling from an emitter to a detector. The sensors of the operational CT scanner (positioned at the emitter and at the detector) then measures, for each X-ray beam, the loss of energy, resulting from the X-ray beam passing through the medium. The loss of energy reflects the ability of the medium to absorb energy, and so it depends on its specific structure and material properties. The amount of absorption can be described as a function of the computational domain Ω, termed

attenuation coefficient function, $f : \Omega \to [0, \infty)$. The primary goal of medical image reconstruction from CT scans is to reconstruct the unknown attenuation coefficient function f from given X-ray scans in order to generate clinically useful medical images. This in turn requires robust numerical algorithms to reconstruct characteristic features of medical images at sufficiently high accuracy, on the one hand, and at sufficiently small computational costs, on the other hand. For details concerning the acquisition of X-ray scans, their underlying mathematical models, and standard computational methods for medical image reconstruction, we refer to the textbook [7] of Feeman.

To describe the mathematical problem of medical image reconstruction from X-ray scans, let us first regard the *Radon transform* $\mathcal{R}f$ of f, given by

$$\mathcal{R}f(t,\theta) = \int_{\mathbb{R}} f(t\cos(\theta) - s\sin(\theta), t\sin(\theta) + s\cos(\theta))\, ds \qquad \text{for } t \in \mathbb{R} \text{ and } \theta \in [0,\pi), \tag{1}$$

where we assume that $f : \Omega \to \mathbb{R}$ is a bivariate function on a compact domain $\Omega \subset \mathbb{R}^2$, or, in other words, we assume that f is compactly supported on $\mathbb{R}^2$, where we extend f to $\mathbb{R}^2$ by letting $f \equiv 0$ outside Ω. In many relevant application scenarios, we may assume that the image domain Ω is the unit square, i.e., $\Omega = [0,1]^2$, but this restriction is rather immaterial for our following discussion. We will merely assume $f \in L^1$, so that for any pair of $t \in \mathbb{R}$ and $\theta \in [0,\pi)$ the Radon integral in (1) is well-defined.

We remark that the Radon transform $\mathcal{R}f(t,\theta)$ gives, for any fixed pair $(t,\theta) \in \mathbb{R} \times [0,\pi)$, a line integral for f over a specific straight line $\ell \equiv \ell_{t,\theta}$. In order to see this, let $\ell_{t,\theta} \subset \mathbb{R}^2$ denote the unique straight line, which is perpendicular to the unit vector $\vec{n} = (\cos(\theta), \sin(\theta))$ and which passes through the point $p = (t\cos(\theta), t\sin(\theta))$. In this case, the line $\ell_{t,\theta}$ can be parameterized as

$$(x(s), y(s)) = p + s\vec{v} = (t\cos(\theta) - s\sin(\theta), t\sin(\theta) + s\cos(\theta)) \qquad \text{for } s \in \mathbb{R}, \tag{2}$$

where we let $\vec{v} = (-\sin\theta, \cos\theta)$, so that $\vec{v} \perp \vec{n}$. By this specific choice for a parameterization of $\ell_{t,\theta}$ in (2), we immediately see that

$$\int_{\ell_{t,\theta}} f(x_1,x_2)\, dx_1\, dx_2 = \int_{\mathbb{R}} f(t\cos(\theta) - s\sin(\theta), t\sin(\theta) + s\cos(\theta))\, ds = \mathcal{R}f(t,\theta)$$

for any $t \in \mathbb{R}$ and $\theta \in [0,\pi)$, and so the line integral of f over $\ell_{t,\theta}$ coincides with the Radon transform (1) of f at (t,θ).

On the other hand, any straight line ℓ in the plane can be described by a unique pair (t,θ) of a radial parameter $t \in \mathbb{R}$ and an angular parameter $\theta \in [0,\pi)$ satisfying $\ell \equiv \ell_{t,\theta}$. In this way, the Radon transform $\mathcal{R}f$ of f can be viewed as a transformation, which maps any bivariate function $f \in L^1$ (in Cartesian coordinates) onto a bivariate function $\mathcal{R}f$ (in polar coordinates), where the image $\mathcal{R}f$ contains all line integrals of f over the set of straight lines in the plane.

Due the seminal work [14] of Johann Radon (in 1917), any (sufficiently regular) function f can be reconstructed from its Radon transform $\mathcal{R}f$. The inversion of the Radon transform is given by the *filtered back projection* (FBP) formula (see [7, Chapter 6]),

$$f(x_1,x_2) = \frac{1}{2}\mathcal{B}\left\{\mathcal{F}^{-1}\left[|S|\mathcal{F}(\mathcal{R}f)(S,\theta)\right]\right\}(x_1,x_2), \tag{3}$$

where $\mathcal{F}$ is, for any fixed angle θ, the *univariate* Fourier transform w.r.t. the radial variable t, and so is $\mathcal{F}^{-1}$ the univariate inverse Fourier transform w.r.t. the frequency variable S. Moreover, the *back projection* $\mathcal{B}$ is, for any function $h \equiv h(t,\theta)$ (in polar coordinates), given by the average

$$\mathcal{B}h(x_1,x_2) = \frac{1}{\pi}\int_0^\pi h(x_1\cos(\theta) + x_2\sin(\theta), \theta)\, d\theta \qquad \text{for } (x_1,x_2) \in \mathbb{R}^2$$

of $h(t,\theta)$ over the angular variable θ, where we let $t = x_1\cos(\theta) + x_2\sin(\theta)$ according to the one-to-one relation between the Cartesian coordinates (x_1, x_2) and the polar coordinates (t,θ), as described above along with the parameterization of the lines $\ell_{t,\theta}$ in (2). For basic details concerning the derivation of the filtered back projection formula, we refer to [7], and for a more comprehensive mathematical treatment of the Radon transform and its inversion, we refer to the textbooks [9, 12].

In practical application scenarios, however, only a *finite* set of Radon data,

$$\mathcal{R}_{\mathcal{L}}(f) = \{\mathcal{R}f(t_k,\theta_k)\}_{k=1}^m, \tag{4}$$

given as integrals of f over a finite set of m pairwise distinct lines,

$$\mathcal{L} = \{\ell_{t_k,\theta_k} : (t_k,\theta_k) \in \mathbb{R}\times[0,\infty) \text{ for } k = 1,\dots,m\},$$

is available. In this case, an approximate reconstruction of f from Radon data $\mathcal{R}_{\mathcal{L}}f$ is sought. In standard techniques of medical imaging, the reconstruction of f is accomplished by using a suitable discretization of the FBP in (3). For this class of Fourier-based reconstruction methods, the discrete lines in $\mathcal{L}$, over which the line integrals of f are known, are usually required to be regularly spaced in the plane, e.g. by assuming *parallel beam geometry* or *fan beam geometry* (see [7] for details concerning these particular assumptions on the geometry of $\mathcal{L}$).

In many clinical scenarios of data acquisition, however, we may face a limited range of angles (e.g. in mammography), or a limited dosage of X-ray expositions, so that the Radon data are partly corrupt or incomplete. In such relevant cases, the Radon data in (4) are typically *scattered*, i.e., the lines in $\mathcal{L}$ are scattered, in which case standard Fourier methods do no longer apply. This may also be relevant in situations, where sensitive regions, e.g. optical nerves or the spinal column, are being scanned, or when it comes to scanning regions of the body containing artifact inducting materials, such as stainless steel hips. In all such possible application scenarios, we are essentially concerned with the approximation of f from *scattered* (Radon) data $\mathcal{R}_{\mathcal{L}}f$.

One way for doing so is to first compute an interpolation to the Radon data in (4), before a Fourier-based FBP discretization is applied, as this has recently been suggested by Beatson and zu Castell in [2]. Other possible reconstruction methods are relying on wavelets (e.g. [3, 6]).

Algebraic reconstruction techniques (ART) [8] are fundamentally different from Fourier-based (or wavelet-based) reconstructions. In the setting of ART, one fixes a suitable set $\mathcal{S} = \{s_j\}_{j=1}^n$ of basis functions beforehand to solve the reconstruction problem

$$\mathcal{R}_{\mathcal{L}}(s) = \mathcal{R}_{\mathcal{L}}(f) \tag{5}$$

by using a linear combination

$$s = \sum_{j=1}^n c_j s_j$$

of the basis functions in $\mathcal{S}$, where n may be the number of pixels in the image representation. This ansatz amounts to solving the linear system

$$Ac = b \tag{6}$$

for the unknown coefficients $c = (c_1,\dots,c_n)^T \in \mathbb{R}^n$ of s, where the $m\times n$ matrix A has the form

$$A = (\mathcal{R}s_j(t_k,\theta_k))_{k=1,\dots,m;j=1,\dots,n} \in \mathbb{R}^{m\times n}$$

and the right hand side b is given by the m Radon observations $b_k = \mathcal{R}f(t_k,\theta_k)$, for $k = 1,\dots,m$.

Unless the number m of Radon samples coincides with the number n of coefficients, the linear system in (6) is either overdetermined, for $m > n$, or underdetermined, for $n > m$. In case of an overdetermined system, the classical method of *linear least squares approximation* [4] is applied to minimize the residual (Euclidean) norm $\|Ac - b\|$, whereas for an underdetermined system the iterative method of Kaczmarz [7, Section 9.3] is a standard tool to compute an approximate solution c satisfying $Ac \approx b$. We remark that in either case the linear system in (6) is not guaranteed to have a unique solution, not even in the rare case, where $m = n$. In fact, the latter is due to the *Mairhuber theorem* [5, Chapter 1] from multivariate approximation theory.

In this paper, we propose a kernel-based algebraic reconstruction method, whose solution is always unique. To this end, we use positive kernel functions to obtain a square system of the form (6) with a symmetric and positive definite matrix A, where the basis functions in $\mathcal{S} = \{s_j\}_{j=1}^n$ do essentially depend on the given Radon functionals $\mathcal{R}_\mathcal{L}$. Our proposed reconstruction scheme relies on the general theory of kernel-based multivariate interpolation from generalized Hermite-Birkhoff data [10], where we adapt this particular interpolation scheme to the special case of reconstruction from scattered Radon data. But in order to ensure well-defined entries in the reconstruction matrix A, we need to apply weighted Radon transforms for the purpose of regularization, as explained later in this paper. This way we obtain a well-posed reconstruction scheme, which works for arbitrary scattered Radon data.

The outline of this paper is as follows. In the following Section 2, we briefly review the solution to the generalized Hermite-Birkhoff interpolation problem, where we show how to adapt that scheme to the special case of reconstruction from scattered Radon data. This is followed by a discussion in Section 3 concerning the regularization of the Radon transform, where we work with weighted Radon transforms. In Section 4, numerical results are finally provided for illustration. Our numerical experiments of Section 4 include comparisons between Fourier-based reconstructions relying on the FBP formula and the kernel-based ART proposed in this paper, where we apply the two different reconstructions to commonly used phantoms.

2 Generalized Hermite-Birkhoff Interpolation

To solve the reconstruction problem (5), we consider applying Hermite-Birkhoff interpolation [10]. To explain the general framework of this particular interpolation method, let $\Lambda = \{\lambda_1, \ldots, \lambda_n\}$ denote a set of linearly independent linear functionals. Moreover, suppose we are given a vector $f_\Lambda = (\lambda_1(f), \ldots, \lambda_n(f))^T \in \mathbb{R}^n$ of samples taken from an unknown function f. Now the solution of the general Hermite-Birkhoff reconstruction problem requires finding a function s satisfying the interpolation conditions $s_\Lambda = f_\Lambda$, i.e.,

$$\lambda_k(s) = \lambda_k(f) \qquad \text{for all } k = 1, \ldots, n. \tag{7}$$

Note that this general framework covers our reconstruction problem when the linear functionals λ_k are defined as

$$\lambda_k(f) := \mathcal{R}f(t_k, \theta_k) \qquad \text{for } k = 1, \ldots, n. \tag{8}$$

By the interpolation conditions in (7), we obtain n linear equations of the form

$$\sum_{j=1}^{n} c_j \lambda_k(s_j) = \lambda_k(f) \qquad \text{for } k = 1, \ldots, n,$$

corresponding to the linear system in (6). But by the choice of our particular ansatz, the number of data matches the number of basis functions, i.e., we have $n = m$.

Now in order to obtain a well-posed interpolation scheme, we require that the basis functions s_j are of the form

$$s_j(x) = \lambda_j^y K(x,y) \qquad \text{for } j = 1, \ldots, n, \tag{9}$$

where $\lambda_j^y K(x,y)$ denotes action of the functional λ_j to K w.r.t. variable y. Moreover, the kernel function $K \equiv K(x,y)$ is required to be symmetric and positive definite. For a more recent account to the construction and characterization of positive definite kernels, we refer the reader to [11]. For the purposes of this paper, it is sufficient to say that K is a symmetric and positive definite kernel, iff the matrix

$$A = \left(\lambda_j^x \lambda_k^y K(x,y)\right)_{1 \le j,k \le n} \in \mathbb{R}^{n \times n}$$

is symmetric and positive definite for any set $\Lambda = \{\lambda_j\}_{j=1}^n$ of linearly independent functionals λ_j.

To make relevant examples for positive definite kernels, we resort to radially symmetric kernels, in which case K is assumed to have the form

$$K(x,y) = \phi(\|x - y\|) \qquad \text{for } x, y \in \mathbb{R}^d,$$

where $\phi : [0, \infty) \to \mathbb{R}$ is radial w.r.t. the Euclidean norm $\|\cdot\|$.

Example 1. The *Gaussian* function

$$\phi_\varepsilon(r) = e^{-(\varepsilon r)^2} \qquad \text{for } r \in [0, \infty) \text{ and } \varepsilon > 0$$

is for any $\varepsilon > 0$ positive definite, i.e., $K(x,y) = \exp(-(\varepsilon \|x - y\|)^2)$ is positive definite.

Example 2. The *inverse multiquadric*

$$\phi_\varepsilon(r) = \left(1 + (\varepsilon r)^2\right)^{-1/2} \qquad \text{for } r \in [0, \infty) \text{ and } \varepsilon > 0$$

is for any $\varepsilon > 0$ positive definite, i.e., $K(x,y) = 1/\sqrt{1 + (\varepsilon \|x - y\|)^2}$ is positive definite.

Example 3. The compactly supported *radial characteristic functions* of Askey [1],

$$\phi_\varepsilon(r) = (1 - \varepsilon r)_+^\beta = \begin{cases} (1 - \varepsilon r)^\beta & \text{for } r < 1/\varepsilon \\ 0 & \text{for } r \ge 1/\varepsilon \end{cases} \qquad \text{for } r \in [0, \infty) \text{ and } \varepsilon > 0,$$

are for any $\beta > 3/2$ positive definite on $\mathbb{R}^2$.

For all three choices of functions ϕ_ε, from Examples 1-3, the resulting linear system has a symmetric and positive definite reconstruction matrix

$$A = \left(\lambda_j^x \lambda_k^y K(x,y)\right)_{1 \le j,k \le n} \in \mathbb{R}^{n \times n},$$

where we have tacitly assumed that all entries $\lambda_j^x \lambda_k^y K(x,y)$ in A are well-defined. This assumption, however, may be too sloppy, especially when the input data $\lambda_k(f)$ in (8) are generated by Radon transforms. We describe and address the resulting problems in the following section.

3 Regularization by Weighted Radon Transforms

The Hermite-Birkhoff interpolation method from Section 2 can, in general, not be applied to the reconstruction from scattered Radon data. In fact, at least two problems may occur, that we can describe and solve as follows.

Problem 1: Singular basis functions. Note that the Radon transform

$$\mathcal{R}^y K(x,y)(t,\theta) = \int_{\mathbb{R}} K(x, (t\cos(\theta) - s\sin(\theta), t\sin(\theta) + s\cos(\theta)))\, ds \tag{10}$$

of the basis functions in (9) may be undefined for specific choices of $(t,\theta) \in \mathbb{R} \times [0,\pi)$ and $x \in \mathbb{R}^2$. To make one example, we regard the inverse multiquadric

$$K(x,y) = (1 + (\varepsilon\|x-y\|)^2)^{-1/2} = \mathcal{O}(\|y\|^{-1}) \quad \text{for } \|y\| \to \infty$$

In this case, we have

$$K(x, (t\cos(\theta) - s\sin(\theta), t\sin(\theta) + s\cos(\theta))) = \mathcal{O}(s^{-1}) \quad \text{for } s \to \pm\infty,$$

so that the integral in (10) is singular for any $(t,\theta) \in \mathbb{R} \times [0,\pi)$ and $x \in \mathbb{R}^2$.

Solution 1: To solve this problem, we apply a *Gabor transform*, with window function

$$G_\sigma(r) = \frac{1}{\sqrt{2\pi}\sigma} \exp\left(-\frac{r^2}{2\sigma^2}\right) \qquad \text{for } \sigma > 0,$$

to the kernel $K(x,y) = \phi_\varepsilon(\|x-y\|)$, i.e., we replace the radial kernel ϕ_ε in the reconstruction scheme of Section 2 by the windowed inverse multiquadric kernel

$$\phi_{\varepsilon,\sigma}(r) := \phi_\varepsilon(r) G_\sigma(r),$$

where the width $2\sigma > 0$ of the Gabor window G_σ is chosen to match the diameter of the computational domain, i.e., we let $\sigma := \operatorname{diam}(\Omega)/2$. Note that $\phi_{\varepsilon,\sigma}$ is positive definite, since each factor, ϕ_ε and G_σ, is positive definite, i.e., $\phi_{\varepsilon,\sigma}$ is for any $\varepsilon, \sigma > 0$ a positive definite radial kernel function. In this way, we obtain a well-defined integral (10), since the integrand

$$K(x,y) = \phi_{\varepsilon,\sigma}(\|x-y\|) = \frac{1}{\sqrt{2\pi}\sigma} \frac{\exp\left(-\frac{\|x-y\|^2}{2\sigma^2}\right)}{\sqrt{1 + (\varepsilon\|x-y\|)^2}}$$

is for any $x \in \mathbb{R}^2$ in $L^1(\mathbb{R}^2)$ w.r.t. variable $y \equiv y(s) = (t\cos(\theta) - s\sin(\theta), t\sin(\theta) + s\cos(\theta))$.

Note that for the other two choices of kernel functions, i.e., for the Gaussians (Example 1) and for the radial characteristic functions (Example 3), this problem does not occur. Indeed, in either of these two cases, we have $\phi_\varepsilon(r) \in L^1([0,\infty))$, so that the function $K(x,\cdot) = \phi_\varepsilon(\|x - \cdot\|)$ is, for any $\varepsilon > 0$ and $x \in \mathbb{R}^2$, integrable over $\mathbb{R}^2$. In particular, the integral in (10) is in this case well-defined for any combination of $(t,\theta) \in \mathbb{R} \times [0,\pi)$ and $x \in \mathbb{R}^2$. We have computed their basis functions in [16] as follows.

Example 4. The basis functions s_j in (9) from the Gaussian kernel (of Example 1) are given as

$$(\mathcal{R}^y K(x,y))(t_j,\theta_j) = \frac{\sqrt{\pi}}{\varepsilon} e^{-\varepsilon^2 (t_j - x\cdot\vec{n}_j)^2} \qquad \text{for } \vec{n}_j = (\cos(\theta_j), \sin(\theta_j)).$$

Details on our computations can be found in [16, Section 5.1.3].

Example 5. The basis functions s_j in (9) from the compactly supported kernel $\phi_\varepsilon(r) = (1-\varepsilon r)_+^2$ (of Example 3 for $\beta = 2$) are given as

$$(\mathcal{R}^y K(x,y))(t_j,\theta_j) = \begin{cases} g(t_j - x\cdot\vec{n}_j) & \text{for } |t_j - x\cdot\vec{n}_j| \le 1/\varepsilon, \\ 0 & \text{for } |t_j - x\cdot\vec{n}_j| > 1/\varepsilon, \end{cases}$$

where $\vec{n}_j = (\cos(\theta_j), \sin(\theta_j))$, and where

$$g(t) = \begin{cases} \frac{2}{\varepsilon}\left[\frac{\sqrt{1-(\varepsilon t)^2}}{3}(2(\varepsilon t)^2+1) - (\varepsilon t)^2 \operatorname{acosh}(\varepsilon^{-1}|t|^{-1})\right] & \text{for } t \neq 0, \\ \frac{2}{3\varepsilon} & \text{for } t = 0. \end{cases}$$

Details on our computations can be found in [16, Section 5.4.1].

Problem 2: Singular entries in the reconstruction matrices. Even if we may assume that the basis functions $s_j = (\mathcal{R}^y K(\cdot, y))(t_j, \theta_j)$ in (9) are well-defined for $(t_j, \theta_j) \in \mathbb{R} \times [0, \pi)$, their Radon transforms $\mathcal{R}^x[(\mathcal{R}^y K(x, y))(t_j, \theta_j)](t_k, \theta_k)$ may be undefined, in which case individual entries

$$a_{kj} = \mathcal{R}^x[(\mathcal{R}^y K(x, y))(t_j, \theta_j)](t_k, \theta_k)$$

in the reconstruction matrix $A = (a_{kj})_{1 \leq j,k \leq n}$ may be undefined. To make one example, consider the basis functions from the Gaussian kernel (see Example 4) . In this case, the matrix entries are given as

$$a_{kj} = \begin{cases} \frac{\pi}{\varepsilon^2 \sin(\theta_k - \theta_j)} & \text{for } \theta_k \neq \theta_j, \\ +\infty & \text{for } \theta_k = \theta_j, \end{cases}$$

cf. our computation in [16, Section 5.1]. Therefore, all diagonal entries a_{jj}, $1 \leq j \leq n$, are singular.

Solution 2: We solve this problem by the application of standard regularization techniques. To this end, we multiply the basis functions $s_j(x) = \mathcal{R}^y K(x, y)(t_j, \theta_j)$ by a non-negative weight function $w(x)$ satisfying

$$\mathcal{R}[s_j(x)w(x)](t, \theta) < \infty \qquad \text{for all } (t, \theta) \in \mathbb{R} \times [0, \pi)$$

for all $1 \leq j \leq n$. Note that this corresponds to a regularization of the Radon operator $\mathcal{R}$. In other words, we replace, for fixed weight function $w \equiv w(x)$, the Radon transform $\mathcal{R}$ by the *weighted Radon transform* $\mathcal{R}_w$, defined as

$$\mathcal{R}_w f(t, \theta) := \mathcal{R}(fw)(t, \theta) = \int_{\ell_{t,\theta}} f(x)w(x)\, dx \qquad \text{for all } (t, \theta) \in \mathbb{R} \times [0, \pi). \tag{11}$$

We remark that the weighted Radon transform arises in relevant applications of single photon emission computed tomography (SPECT), where $\mathcal{R}_w$ is called *attenuated Radon transform* [13].

The application of the proposed regularization leads us to the modified reconstruction problem

$$\mathcal{R}_w s(t_k, \theta_k) = \mathcal{R} f(t_k, \theta_k) \qquad \text{for all } k = 1, \ldots, n,$$

with assuming (9) for the form of the basis functions s_j, so that

$$s(x) = \sum_{j=1}^{n} c_j s_j(x) = \sum_{j=1}^{n} c_j (\mathcal{R}^y K(x, y))(t_j, \theta_j)$$

gives the form of the reconstruction s. The unknown coefficients $c = (c_1, \ldots, c_n)^T \in \mathbb{R}^n$ of s are given by the solution of the linear system (6), but now with the regularized reconstruction matrix

$$A \equiv A_w = (\mathcal{R}_w s_j(t_k, \theta_k))_{1 \leq j,k \leq n} \in \mathbb{R}^{n \times n}. \tag{12}$$

Now let us finally turn to the choice of the weight function w. The weight w is usually a function of variables x and θ. But in our case, it will be convenient to assume that w does only depend on the Euclidean norm of variable x, i.e., $w \equiv w(\|x\|)$. In our numerical experiments, we have considered using two families of weight functions w_ν, where ν is a positive scale parameter:

- the Gaussian weight function

$$w_\nu(x) = \exp(-(\nu\|x\|)^2) \quad \text{for } x \in \mathbb{R}^2, \tag{13}$$

- the compactly supported weight function

$$w_\nu(x) = (1-(\nu\|x\|)^2)_+ = \begin{cases} 1-(\nu\|x\|)^2 & \text{for } \|x\| < 1/\nu, \\ 0 & \text{for } \|x\| \geq 1/\nu, \end{cases} \quad \text{for } x \in \mathbb{R}^2. \tag{14}$$

By our choices of kernels (from Examples 1-3) and weight functions (13)-(14), we can compute the weighted Radon transforms $\mathcal{R}_w(s_j)$ in (11) analytically. In this way, we obtain explicit expressions for the entries of the reconstruction matrix A in (12). For the Gaussian kernel ϕ_ε of Example 1, for instance, we apply the Gaussian weight function $w_\nu(x) = \exp(-(\nu\|x\|)^2)$, in which case we can compute the entries in A as

$$a_{kj} = \mathcal{R}_w s_j(t_k, \theta_k) = \frac{\pi \exp\left[-\nu^2\left(t_k^2 + \frac{(\varepsilon\beta_{kj})^2}{(\varepsilon\alpha_{kj})^2+\nu^2}\right)\right]}{\varepsilon\sqrt{(\varepsilon\alpha_{kj})^2+\nu^2}},$$

where we let $\beta_{kj} = t_k - t_j\cos(\theta_k-\theta_j)$ and $\alpha_{kj} = \sin(\theta_k-\theta_j)$. Details on our computations can be found in [16, Section 5], where also other relevant combinations of kernels ϕ_ε and weight functions w_ν are covered.

4 Numerical Results

We have implemented the proposed kernel-based reconstruction scheme for the three kernels ϕ_ε from Examples 1-3 in combination with the Radon transform's regularization, by using the two weight functions w_ν in (13)-(14). We have performed quite comprehensive numerical experiments for various possible combinations of kernels ϕ_ε and weights w_ν, a small selection of which we present here for the purpose of illustration.

In our series of numerical experiments concerning the popular phantoms *bull's eye*, the *crescent-shaped phantom*, and the *Shepp-Logan phantom*, we found that the Gaussian kernel (Example 1) performs much better than the inverse multiquadric (Example 2) and the compactly supported kernel $\phi_\varepsilon(r) = (1-\varepsilon r)_+^2$ (Example 3 for $\beta = 2$), where the performance of the latter two kernels is comparable. This is supported by our numerical example in Figure 5. Indeed, we obtained the best numerical results – in terms of the reconstructions' visual quality and the root mean square error (RMSE) in (15) – for the Gaussian kernel $\phi_\varepsilon(r) = \exp(-(\varepsilon r)^2)$ in combination with the Gaussian weight function $w_\nu(x) = \exp(-(\nu\|x\|)^2)$, provided that the shape parameters ε and ν were properly chosen.

In fact, we found that the performance of the Gaussian reconstruction method is quite sensitive to the choice of the method parameters ε and ν. Therefore, we decided to perform a "fine-tuning" of the Gaussian parameters ε and ν, whose numerical results are presented in Subsection 4.2. Moreover, in Subsection 4.3 we provide numerical comparisons with Fourier-based reconstructions, relying on the filtered back projection formula, for Radon data on parallel beam geometry. In Subsection 4.4, we present numerical results concerning Gaussian reconstruction from *scattered* Radon data, and in Subsection 4.5 from *regular* Radon data (on parallel beam geometry), where we also provide a comparison between different kernels. Comparisons concerning Gaussian reconstruction on regular Radon data vs scattered Radon data are provided in the following Subsection 4.1. For a more comprehensive documentation on our numerical experiments, we refer to [16].

4.1 Gaussian Reconstruction of the Crescent-Shaped Phantom

Let us first regard the popular test case *crescent-shaped phantom*, given by the function

$$f(x,y) = \begin{cases} 1.0 & \text{for } (x,y) \in \Omega, \\ 0.5 & \text{for } (x,y) \in D_i, \\ 0.0 & \text{for } (x,y) \in \mathbb{R}^2 \setminus D_o, \end{cases}$$

on the unit square $\Omega = [0,1]^2$, where

$$D_i = \{(x,y) \in \mathbb{R}^2 : (x-1/8)^2 + y^2 \leq 9/64\} \quad \text{and} \quad D_o = \{(x,y) \in \mathbb{R}^2 : x^2 + y^2 \leq 1/4\},$$

as shown in Figure 1 (a).

Figures 1 (b),(c) show the reconstruction of the crescent-shaped phantom obtained with the Gaussian kernel ϕ_ε and the Gaussian weight function w_ν for parameters $\varepsilon = 40$ and $\nu = 0.7$, and for $n = 3888$ different Radon lines. The Radon samples were taken on a set of n regularly distributed lines generated by *parallel beam geometry*, and on a set of n *scattered* Radon lines. In either case, the crescent-shaped phantom f is localized and reconstructed fairly well by the proposed kernel-based reconstruction scheme. But the quality of the reconstruction on parallel beams, Figure 1 (b), is superior to that on scattered lines, Figure 1 (c). This is due to the uniform coverage of the Radon lines over the computational domain Ω. The geometry of the Radon lines are visible in the display of the reconstructions in Figures 1 (b),(c), especially between the boundary of the domain Ω and the phantom's boundary.

(a) crescent-shaped phantom (b) parallel beam geometry (c) scattered Radon data

Figure 1: **Crescent-shaped phantom.** (a) Original phantom; (b)-(c) reconstruction of crescent-shaped phantom using the Gaussian kernel ϕ_ε with $\varepsilon = 40$ and the Gaussian weight function w_ν with $\nu = 0.7$ from $n = 3888$ Radon samples taken on (b) regularly spaced Radon lines (parallel beam geometry), (c) scattered Radon lines.

4.2 On the Selection of the Gaussian Shape Parameters

In this subsection, we discuss the variation of the method parameters ε (for the Gaussian kernel ϕ_ε) and ν (for the Gaussian weight function w_ν), where we use the phantom *bull's eye*, whose radially symmetric test function is given as

$$f(x,y) = \begin{cases} 1/2 & \text{iff } x^2 + y^2 \leq 1/16; \\ 1/4 & \text{iff } 1/16 < x^2 + y^2 \leq 1/4; \\ 1 & \text{iff } 1/4 < x^2 + y^2 \leq 9/16; \\ 0 & \text{iff } 9/16 < x^2 + y^2. \end{cases}$$

The phantom bull's eye is displayed in Figure 5, second row, first column. In our numerical experiments, we have analyzed the behaviour of the Gaussian reconstruction error as a bivariate function of parameters ε and ν. For the error measure, we consider using the standard *root mean square error*

$$\text{RMSE} = \sqrt{\frac{1}{J}\sum_{j=1}^{J}(f_j - \hat{f}_j)^2}, \tag{15}$$

where J is the size of the image (i.e., the number of pixels) and $\{f_j\}_{j=1}^J$, $\{\hat{f}_j\}_{j=1}^J$ are the greyscale values at the pixels of the original image bull's eye and of the reconstructed image, respectively.

Let us first consider the variation of the shape parameter ε of the Gaussian kernel ϕ_ε. In our numerical experiments, we have fixed the weight parameter at $\nu = 0.7$. For different choices of N and M, we have used parallel beam geometry with N angles and $2M+1$ parallel lines per angle, resulting in a number of $n = N \times (2M+1)$ Radon samples for each numerical experiment. With the variation of the shape parameter ε, we have recorded an "optimal" value ε^*, where, according to our numerical observations, the RMSE is minimal. The following Table 1 reflects our results. Note that the "optimal" value ε^* increases with the number n of Radon data taken. This is not too surprising insofar as in plain kernel-based interpolation, the shape parameter of the Gaussian kernel is recommended to be proportional to the density of the sample points: the higher the density of points, the larger ε should be chosen. In our numerical experiments, the sample density increases with the number n of lines, which explains the monotonicity of ε^* in Table 1.

N	36	54	72	90	108	126	144	162	180
M	20	30	40	50	60	70	80	90	100
n	1,476	3,294	5,832	9,090	13,068	17,766	23,184	29,322	36,180
ε^*	21.05	28.42	37.36	48.42	59.47	72.10	84.21	90.52	97.37

Table 1: **Parameter-tuning for Gaussian kernel ϕ_ε.** Reconstruction of phantom bull's eye by Gaussian kernel ϕ_ε, with variation of the kernel parameter ε. For fixed weight parameter $\nu = 0.7$, and for different choices of N angles θ and $2M+1$ lines per angle in a parallel beam geometry. For each experiment, the "optimal" shape parameter ε^*, whose resulting RMSE is minimal, is shown.

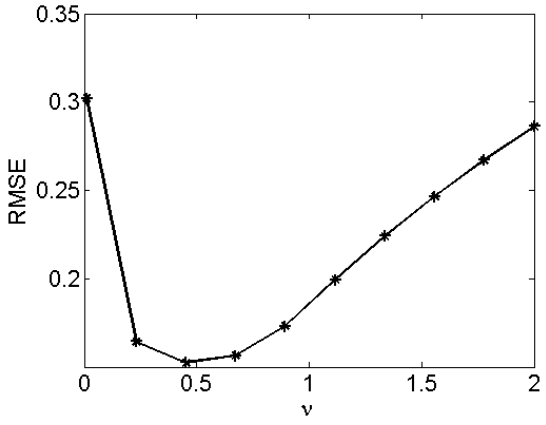

Figure 2: **Parameter-tuning for Gaussian weight function w_ν.** Reconstruction of phantom bull's eye by the Gaussian kernel $\phi_\varepsilon(r) = \exp(-(\varepsilon r)^2)$ for $\varepsilon = 30$. The graph of the RMSE as a function of the weight parameter ν is shown.

Next we consider the variation of the shape parameter ν for the Gaussian weight function w_ν in (13). Figure 2 shows the RMSE as a function of ν, for constant kernel shape parameter $\varepsilon = 30$ and for a fixed number $n = 1230$ of Radon lines (on a parallel beam geometry). We have observed that the minimal RMSE is attained at $\nu^* = 0.4522$ (cf. Figure 2). Note that the graph in Figure 2 illustrates the dependence between the RMSE and the weight parameter ν quite well.

We have further performed a series of rather extensive numerical experiments concerning the phantoms bull's eye, the crescent-shaped phantom, and the Shepp-Logan phantom, where our reconstructions were computed on a parallel beam geometry with $N = 30$ angles and $2M + 1 = 41$ lines per angle, so that the number of Radon samples is $n = 1230$. The following Table 2 shows "optimal" combinations of values ε^* for the Gaussian kernel and ν^* for the Gaussian weight, whose resulting RMSE $\equiv$ RMSE(ε, ν) is minimal.

Phantom	Gaussian kernel ϕ_ε	Gaussian weight w_ν
crescent-shaped phantom	$\varepsilon^* = 19.6552$	$\nu^* = 0.5067$
bull's eye	$\varepsilon^* = 15.5172$	$\nu^* = 0.4522$
Shepp-Logan phantom	$\varepsilon^* = 18.2759$	$\nu^* = 2.0558$

Table 2: **"Optimal" shape parameters for Gaussian kernel and Gaussian weight.** Fine-tuning of shape parameter ε^* and weight parameter ν^* for three different phantoms by Gaussian reconstruction on parallel beam geometry (for $N = 30$ angles and $2M + 1 = 41$ lines per angle).

We have used these "optimal" parameters ε^* and ν^* for the numerical comparisons in Figure 5.

4.3 Comparison of the Kernel-based and the Fourier-based Reconstruction

Now let us compare our kernel-based reconstruction method with Fourier-based reconstructions, relying on the filtered back projection formula. We have studied the behaviour of the RMSE as a function of the number n of Radon samples for a parallel beam geometry. Figure 3 illustrates the performances of the reconstruction by the Gaussian kernel and by a Fourier-based reconstruction, for a sequence of data comprising between $n = 210$ and $n = 4050$ Radon samples, taken from the crescent-shaped phantom. On the basis of our numerical results [16], we can conclude that our kernel-based reconstruction method is competitive to the Fourier-based reconstruction method.

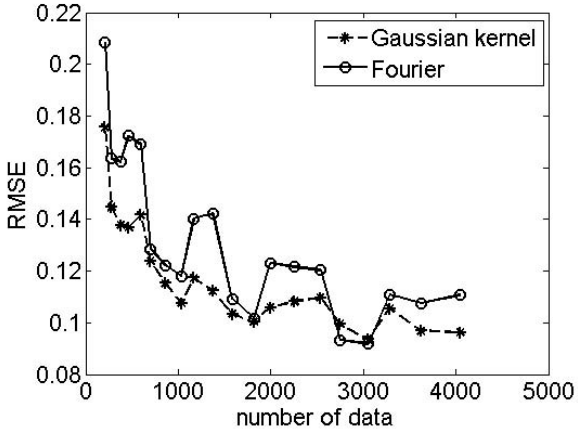

Figure 3: **Reconstruction of crescent-shaped phantom on parallel beam geometry.** RMSE as a function of n Radon samples for a Gaussian kernel and a Fourier-based reconstruction.

4.4 Kernel-based Reconstruction from Scattered Radon Data

Let us finally turn to the reconstruction from *scattered* Radon data. Figure 4 shows a sequence of reconstructions for the phantom bull's eye and for the crescent-shaped phantom, each obtained by applying the Gaussian kernel. Note that the features of the two phantoms are captured fairly well by our kernel-based reconstruction method. Not too surprisingly, the reconstruction quality can be improved by increasing the number n of Radon samples. Particular attention, however, should be paid to the conditioning of the reconstruction matrix A in (12). In fact, the spectral condition number $\kappa(A)$ of A may grow quite rapidly with the number n of samples, especially for scattered Radon data. This in turn affects the stability of the proposed reconstruction algorithm, where the intrinsic correlation between the geometry of the lines in $\mathcal{L}$ and the size of the spectral condition number $\kappa(A)$ is related to Schaback's *uncertainty principle* [15] for plain interpolation. Yet it remains to describe the spectral condition number $\kappa(A)$ as a function of the line geometry.

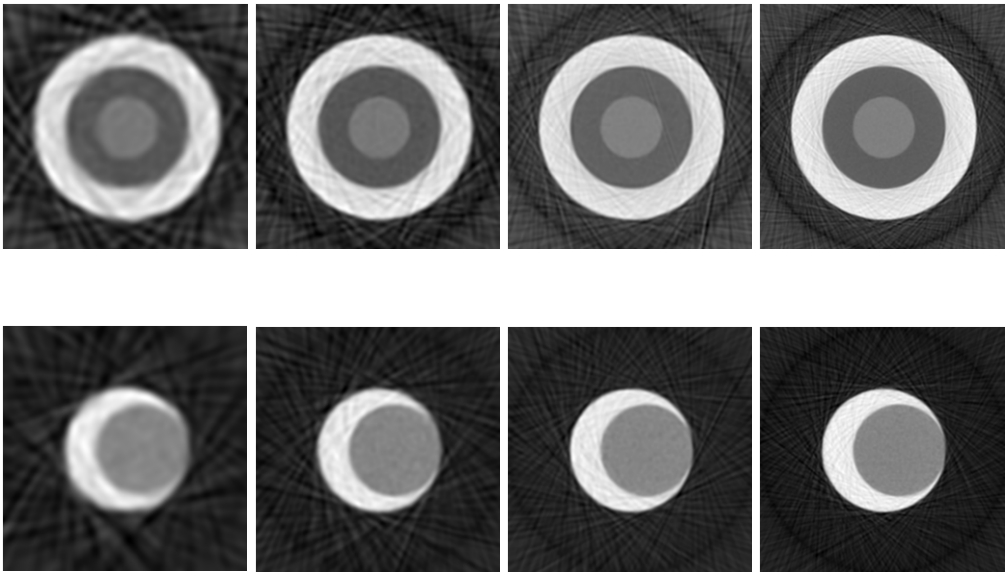

Figure 4: **Scattered data reconstruction by Gaussian kernel.** For the test cases bull's eye (first row) and crescent-shaped phantom (second row), a sequence of scattered Radon data is taken. The figure shows the corresponding reconstructions for an increasing number $n = 2000, 5000, 10000, 20000$ of scattered Radon samples (from left to right).

4.5 Comparison of Kernel-based Reconstructions on Parallel Beam Geometry

We have used the "optimal" Gaussian parameters ε^* and ν^* from Table 2 for the numerical results shown in Figure 5, where a comparison between different kernel functions is made: inverse multiquadric (second column), compactly supported (third column), Gaussian kernel (fourth column). The original phantoms are shown in the first column of Figure 5.

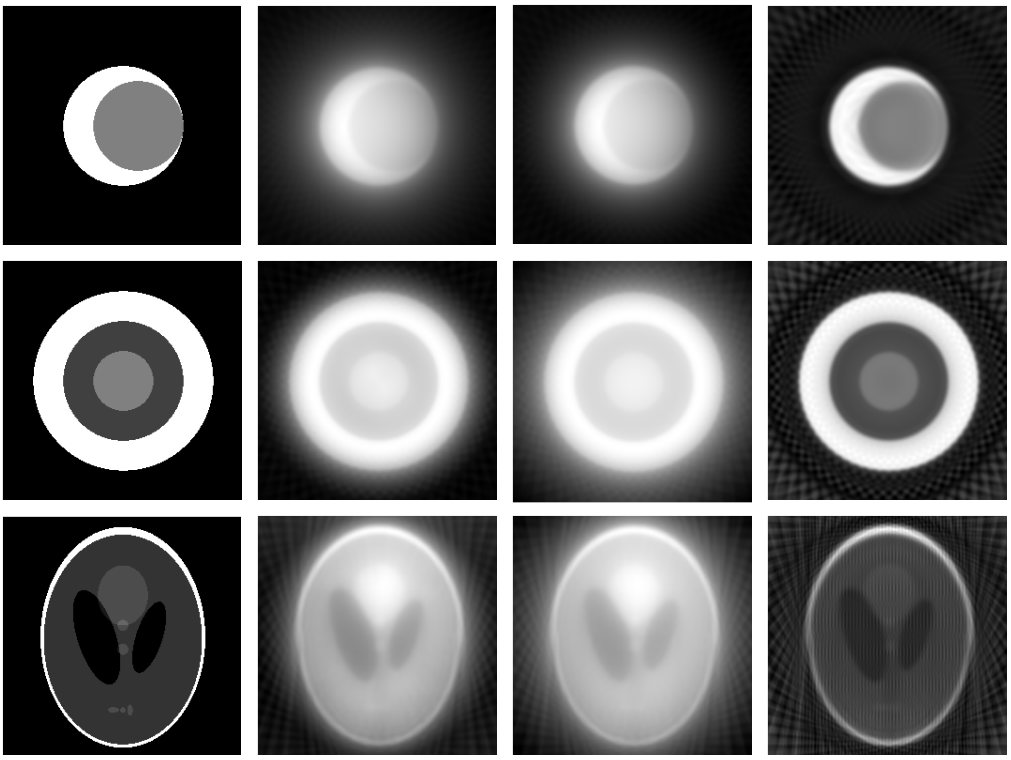

Figure 5: **Kernel-based reconstructions on parallel beam geometry.** The reconstructions are obtained from $n = 1230$ Radon samples, on a parallel beam geometry with $N = 30$ angles and $2M + 1 = 41$ lines per angle. The original phantoms (1st col), their reconstruction by inverse multiquadric (2nd col), by the compactly supported kernel (3rd col), and by the Gaussian kernel (4th col) are shown. The "optimal" values for the Gaussian parameters ε and ν are in Table 2.

On our numerical results of Figure 5 we can conclude that the reconstruction quality obtained from the Gaussian kernel is clearly superior to those obtained from the compactly supported and the inverse multiquadric kernel, provided that the Gaussian method parameters ε and ν are well-chosen. Note that the performance of the compactly supported kernel and the inverse multiquadric kernel is comparable. This complies with our numerical results, as they are documented in [16].

5 Final Remarks and Future Work

We have developed a kernel-based method for (medical) image reconstruction from scattered Radon data. The proposed reconstruction method relies on Hermite-Birkhoff interpolation by positive definite kernel functions, in combination with a weighted regularization of the Radon transform. Our kernel-based reconstruction is very flexible, since it can unconditionally be applied to arbitrary scattered Radon data, unlike classical Fourier-based reconstructions. The behaviour of the shape parameters for the kernel and for the weight function is analyzed in numerical experiments. Our kernel-based reconstruction method is shown to be competitive with Fourier-based reconstructions. On the basis of our numerical results, we give preference to the Gaussian kernel. But the selection of the kernel's shape parameter and the weight parameter requires particular care. Further investigations along these lines should lead to choices of (optimal) kernel shape parameters depending on the geometrical coverage of the Radon lines over the computational domain.

References

[1] R. Askey: Radial characteristic functions. Technical Report, TSR # 1262, University of Wisconsin, Madison, 1973.

[2] R.K. Beatson and W. zu Castell: Scattered data interpolation of Radon data. Calcolo **48**, 2011, 5–19.

[3] M. Bhatia, W.C. Karl, and A.S. Willsky: A wavelet-based method for multiscale tomographic reconstruction. IEEE Trans. Med. Imag. **15**, 1996, 92–101.

[4] Å. Bjørck: *Numerical Methods for Least Squares Problems*. SIAM, Philadelphia, 1996.

[5] W. Cheney and W. Light: *A Course in Approximation Theory*. Brooks/Cole, Pacific Grove, 2000.

[6] B. Dong, J. Li, and Z. Shen: X-ray CT image reconstruction via wavelet frame based regularization and Radon domain inpainting. To appear in *Journal of Scientific Computing*, 2012. DOI: 10.1007/s10915-012-9579-6.

[7] T.G. Feeman: *The Mathematics of Medical Imaging. A Beginner's Guide*. Springer Undergraduate Texts in Mathematics and Technology. Springer, New York, 2010.

[8] R. Gordon, R. Bender, and G. Herman: Algebraic reconstruction techniques (ART) for three dimensional electron microscopy and X-ray photography. Journal of Theoretical Biology **29**(3), 1970, 471–481.

[9] S. Helgason: *The Radon Transform*. Progress in Mathematics, vol. 5, 2nd edition. Birkhäuser, Basel, 1999.

[10] A. Iske: Reconstruction of functions from generalized Hermite-Birkhoff data. In: *Approximation Theory VIII, Vol. 1: Approximation and Interpolation*, C.K. Chui and L.L. Schumaker (eds.), World Scientific, Singapore, 1995, 257–264.

[11] A. Iske: Scattered data approximation by positive definite kernel functions. Rendiconti del Seminario Matematico **69**(3), 2011, 217–246.

[12] F. Natterer: *The Mathematics of Computerized Tomography*. Classics in Applied Mathematics, vol. 32. SIAM, Philadelphia, 2001.

[13] R.G. Novikov: An inversion formula for the attenuated X-ray transformation. Ark. Mat. **40**, 2002, 145–167.

[14] J. Radon: Über die Bestimmung von Funktionen durch ihre Integralwerte längs gewisser Mannigfaltigkeiten. Berichte Sächsische Akademie der Wissenschaften **69**, 1917, 262–277.

[15] R. Schaback: Error estimates and condition numbers for radial basis function interpolation. Advances in Comp. Math. **3**, 1995, 251–264.

[16] A. Sironi: *Medical Image Reconstruction Using Kernel Based Methods. Master's Thesis, University of Padova, 2011. arXiv:1111.5844v1.* `http://arxiv.org/pdf/1111.5844v1.pdf`.